Emergence of dynamic vortex glasses in disordered polar active fluids

Amélie Chardac[a,1], Suraj Shankar[b,1], M. Cristina Marchetti[c], and Denis Bartolo[a,2]

[a]Université de Lyon, École Normale Supérieure de Lyon, Université Claude Bernard, CNRS, Laboratoire de Physique, F-69342 Lyon, France; [b]Department of Physics, Harvard University, Cambridge, MA 02138; and [c]Department of Physics, University of California, Santa Barbara, CA 93106

Edited by David A. Weitz, Harvard University, Cambridge, MA, and approved January 17, 2021 (received for review August 31, 2020)

In equilibrium, disorder conspires with topological defects to redefine the ordered states of matter in systems as diverse as crystals, superconductors, and liquid crystals. Far from equilibrium, however, the consequences of quenched disorder on active condensed matter remain virtually uncharted. Here, we reveal a state of strongly disordered active matter with no counterparts in equilibrium: a dynamical vortex glass. Combining microfluidic experiments and theory, we show how colloidal flocks collectively cruise through disordered environments without relaxing the topological singularities of their flows. The resulting state is highly dynamical but the flow patterns, shaped by a finite density of frozen vortices, are stationary and exponentially degenerated. Quenched isotropic disorder acts as a random gauge field turning active liquids into dynamical vortex glasses. We argue that this robust mechanism should shape the collective dynamics of a broad class of disordered active matter, from synthetic active nematics to collections of living cells exploring heterogeneous media.

active matter | Quincke rollers | disordered media | topological defects

From a physicist's perspective, flocks are ensembles of living or synthetic motile units collectively moving along a common emerging direction (1–4). They realize one of the most robust ordered states of matter observed over five orders of magnitude in scale and in systems as diverse as motility assays, self-propelled colloids, shaken grains, and actual flocks of birds (3, 5–10). The quiet flows of flocks are in stark contrast with the spatiotemporal chaos consistently reported and predicted in active nematic liquid crystals, another abundant form of ordered active matter realized in biological tissues, swimming cells, cellular extracts, and shaken rods (2, 11). Active nematics do not support any form of long-range order (4, 12). Their structure is continuously bent and destroyed by the proliferation and annihilation of singularities in their local orientation: topological defects (11, 13–15). Unlike in active nematics, topological defects in flocking matter are merely transient excitations which annihilate rapidly and allow uniaxial order to extend over system-spanning scales (4).

This idyllic view of the ordered phases of active liquids is limited, however, to pure systems. Disorder is known to profoundly alter the stability of topological defects and the corresponding ordered states in equilibrium condensed matter (16–18), but its role in active fluids remains virtually uncharted territory. All previous studies (19–26), including our own early experiments (22), have been limited to weak disorder and smooth perturbations around topologically trivial states. Unlike in equilibrium, no available experiment, simulation, or theory has ever demonstrated or predicted disorder-induced topological excitations in active matter.

In this paper we show how isotropic disorder generically challenges the extreme robustness of flocking matter to topological defects. We map the full phase behavior of colloidal flocks navigating through disordered lattice of obstacles and reveal an unanticipated state of active matter: a dynamical vortex glass. In dynamical vortex glasses, millions of self-propelled particles can steadily cruise through disorder, maintaining local orientational order and without relaxing the topological singularities of their flows. The associated flow patterns are exponentially degenerated and shaped by amorphous ensembles of frozen topological defects, yielding a dynamical state akin to the static vortex-glass phase of dirty superconductors and random-gauge magnets (27–29). Building a theory of flock hydrodynamics beyond the spin-wave approximation, we elucidate the emergence and stabilization of topological vortices by quenched disorder. Finally, we discuss the universality of the dynamical vortex glass phase beyond the specifics of polar active matter and colloidal flocks.

Disordered Flocks on a Chip

Our experiments are based on the model system we introduced in ref. 6. We use Quincke rotation to power inanimate polystyrene beads of radius $a = 2.4\,\mu\mathrm{m}$ (30, 31) and turn them into colloidal rollers self-propelling at constant speed $\sim$1 mm/s in circular microfluidic chambers of radius $R = 1.5\,\mathrm{mm}$ (Fig. 1*A* and Movie S1). Before addressing the impact of disorder on their collective dynamics, it is worth recalling the phenomenology of the pure ordered phase (32, 33).

As the rollers are set in motion they interact and self-assemble into a spontaneously flowing liquid equivalently referred to as a flock, a Toner–Tu fluid, or a polar liquid (2, 34) shown in Movie S1. The resulting flow patterns are initially isotropic and marred by a number of ± 1 topological defects clearly visible in the Schlieren patterns of Fig. 1*A* and Movie S2. However, the

Significance

Active systems, from bacteria to human crowds, often move through disordered environments, but the impact of quenched disorder on self-organized collective flow remains largely unexplored. We combine microfluidic experiments involving a colloidal active fluid and hydrodynamic theory to study a flocking fluid navigating a disordered substrate. While weak disorder hardly disrupts the robust collective motion, above a critical disorder strength the system organizes in a remarkable state of correlated flows through a frozen network of defects—a dynamical vortex glass, akin to vortex glasses in dirty superconductors. Strong disorder and activity conspire to generate a gauge field that proliferates pinned vortices, a general mechanism that may apply to a broad class of synthetic and biological active fluids.

Author contributions: D.B. conceived the project; A.C. and D.B. designed the experiments; A.C. performed the experiments; M.C.M. and S.S. performed the theory; A.C., S.S., M.C.M., and D.B. discussed the results; and A.C., S.S., M.C.M., and D.B. wrote the manuscript.

The authors declare no competing interests.

This article is a PNAS Direct Submission.

[1]A.C. and S.S. contributed equally to this work.

[2]To whom correspondence may be addressed. Email: denis.bartolo@ens-lyon.fr.

This article contains supporting information online at https://www.pnas.org/lookup/suppl/doi:10.1073/pnas.2018218118/-/DCSupplemental.

Published March 3, 2021.

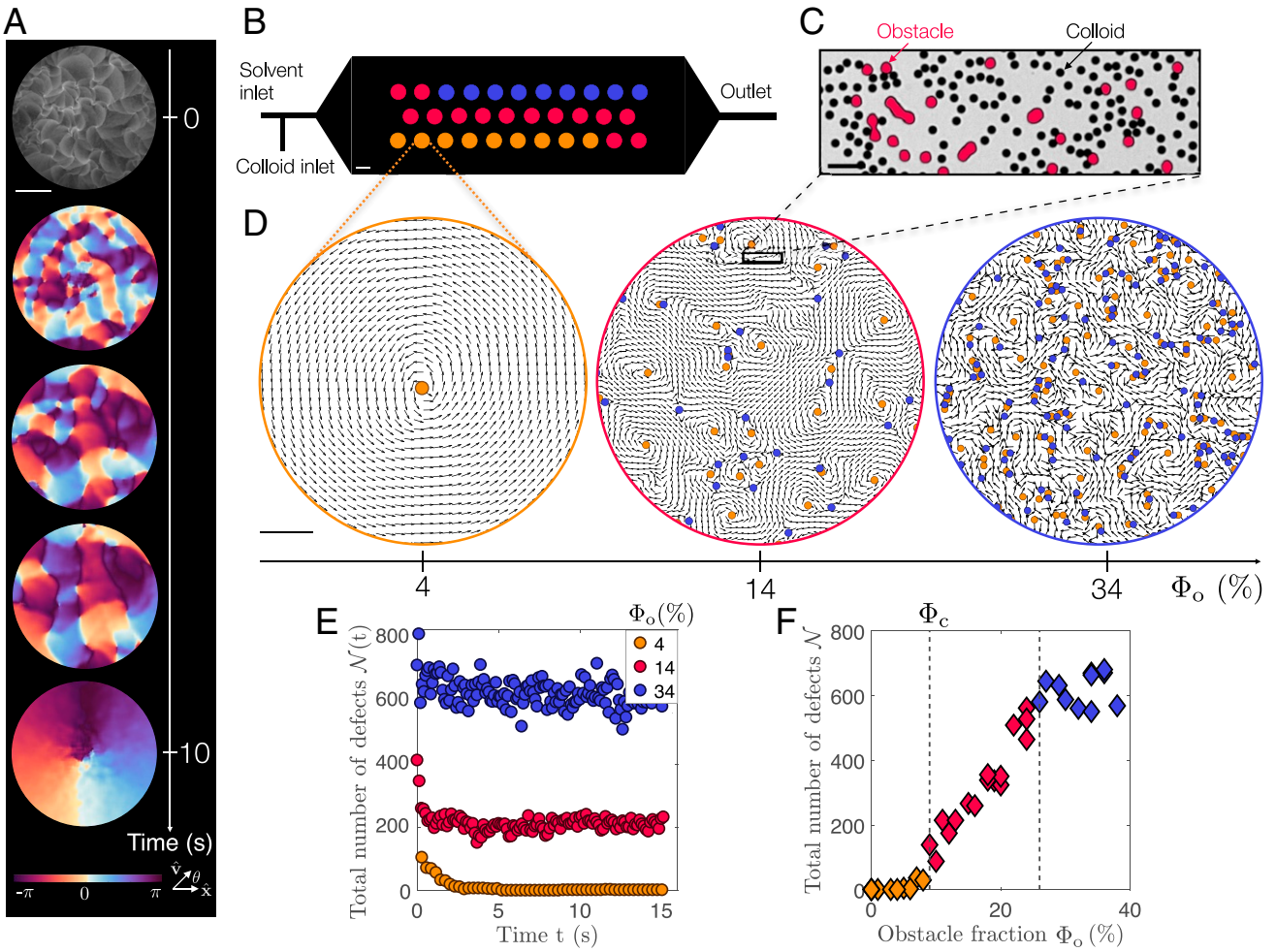

Fig. 1. Emergence and destruction of polar flows. (*A*) Experimental picture of a Quincke-roller fluid at the onset of self-propulsion and subsequent Schlieren patterns of the flow field. The color map indicates the angle of the local velocity field with the *x* axis. The many topological defects formed at the onset of collective motion coarsen, yielding a pristine azimuthal flow. (Scale bar: 1 mm.) (*B*) Schematics of the microfluidic device. Thirty-two circular chambers are patterned with random lattices of circular obstacles. Each chamber corresponds to a different value of Φ_o. A T-junction makes it possible to continuously vary the packing fraction of Quincke rollers in all chambers at once. Same color coding as in *F*. (Scale bar: 3 mm.) (*C*) Close-up picture showing Quincke rollers collectively moving through a disordered lattice of microfabricated obstacles. Obstacles of radius 5 μm are highlighted in pink. (Scale bar: 25 μm.) (*D*) Polarization fields in the vortex, meander, and gas states. The dots indicate the location of the topological defects (orange: +1, blue: −1). (Scale bar: 0.5 mm.) (*E*) Evolution of the number of topological defects $\mathcal{N}(t)$ during the coarsening process for $\Phi_o = 4\,\%$ (polar liquid), $\Phi_o = 14\,\%$ (meander), and $\Phi_o = 34\,\%$ (gas). The error in the number of defect measurement is smaller than the symbol size (see *SI Appendix*). (*F*) Variations of the average number of topological defects in the steady state with the obstacle fraction. The meander phase emerges at $\Phi_c = 9 \pm 1\,\%$.

velocity–alignment interactions responsible for flocking motion penalize flow distortions, thereby causing the attraction and annihilation of defects of opposite charge. The resulting lively coarsening dynamics lasts a few tens of seconds and ultimately yields pristine azimuthal flows with long-range order in two dimensions (Fig. 1*A*).

To comprehensively investigate how disorder alters the phases of polar active matter, we perform high-content experiments on the microfluidic device sketched in Fig. 1*B*. On a single chip, we quantify the flows of disordered roller fluids in 32 different disordered geometries. Disorder is implemented in 3-mm-wide circular chambers which we decorate with random arrays of cylindrical posts of diameter 10 μm and height 2 μm using ultraviolet (UV) lithography. The posts have no spatial correlations (Poissonian distribution). These isotropic obstacles repel the rollers at a distance, while leaving their speed unaltered (see Fig. 1*C* and Movie S3). We replicate the experiments increasing the obstacle area fraction Φ_o from 0 % to 38 %, keeping the system below the Lorentz localization transition of individual rollers (35, 36). All experiments are systematically performed for several disorder realizations and initial conditions (see also *Materials and Methods*).

Let us first discuss the impact of disorder on a polar liquid deep in the flocking phase, for a colloid packing fraction $\rho_0 = 7 \pm 0.5 \times 10^{-2}$. For small disorder, $\Phi_o < 9\,\%$, the obstacles hardly disrupt the collective flow, as ± 1 defects formed at the onset of collective motion quickly annihilate. The system coarsens to an ordered flocking state which, in the disk geometry, takes the form of a macroscopic vortex centered around a single $+1$ defect (see Fig. 1 and Movie S4). In stark contrast, increasing Φ_o above 9 % a very distinct type of organization emerges. Disorder essentially arrests the coarsening by pinning ± 1 defects. While the global flow vanishes, we find locally correlated flows through meandering patterns bent by disorder (Fig. 1*D* and Movies S5 and S6). Particles stream coherently through the meanders, resulting in a finite correlation length for orientational order, but the structure of the flow network itself is static and fixed in space, as shown in Fig. 1*D* and Movie S6. Further increasing the obstacle fraction (above 26 %), we recover the liquid–gas transition reported

in ref. 22. In the gas phase, particles are motile, but there is no orientational order as defect pairs continuously unbind and annihilate as seen in Fig. 1 *D* and *E*. The two transitions between the three dynamical states are unambiguously determined by the variations of $\mathcal{N}(\Phi_o)$, the mean number of topological defects in the velocity field, plotted in Fig. 1*F* (the detection of the topological defects is detailed in *SI Appendix*, section 3). The emergence of meandering flows is signaled by the linear increase of $\mathcal{N}$ as Φ_o exceeds the critical value $\Phi_c = 9\,\%$, whereas the loss of local orientational order saturates $\mathcal{N}(\Phi_o)$ above $\Phi_o = 26\,\%$.

Phase Behavior of Disordered Polar Active Matter

In order to quantitatively distinguish the dynamics in the three regimes we inspect the statistics of the time-averaged polarization defined as $\boldsymbol{p}(\mathbf{r}) = \langle \hat{\mathbf{v}}(\mathbf{r}, t)\rangle_t$, where the unit vector $\hat{\mathbf{v}}(\mathbf{r}, t)$ is the instantaneous orientation of the velocity field (see *Materials and Methods*). The distributions of $\boldsymbol{p}(\mathbf{r})$ in Fig. 2*A* show that, for small disorder, the flow is uniformly polarized along the azimuthal direction, which reflects nearly perfect polar order. Conversely, above Φ_c global polar order is suppressed, and the polarization is isotropically distributed on the scale of the system. The strong localization of the distribution on the unit circle demonstrates, however, that meanders persistently distort the streamlines without arresting the local flows. Above $\Phi_o = 26\,\%$, in the active-gas phase, the typical polarization vanishes, polar order melts, and flows are suppressed at all scales.

We now demonstrate that the two flowing patterns correspond to two distinct dynamical phases. We first stress that polar liquids with genuine long-range orientational order survive at finite disorder (see also *SI Appendix*, section 7). Unlike active nematics, deconfining the system does not suppress the stationary vortex patterns shown in Fig. 1*D* (38–40). This crucial result follows from the finite-size analysis of the polarization order parameter $\mathcal{P}(\ell) = \sqrt{\langle p_r(\mathbf{r})\rangle_{\mathbf{r}}^2 + \langle p_\theta(\mathbf{r})\rangle_{\mathbf{r}}^2}$, where ℓ is the size of the region where spatial averaging is performed. This definition of $\mathcal{P}$ is natural in a circular geometry where the spatial average of $\boldsymbol{p}$ vanishes, even in pure systems. Below Φ_c, *SI Appendix*, Fig. S1 clearly indicates that $\mathcal{P}(\ell)$ converges to a finite value over a finite length scale $\xi_{\mathcal{P}}$, signaling long-range polar order. Conversely, deep in the meandering regime $\mathcal{P}(\ell)$ vanishes over a finite scale. Polar liquids and meanders are therefore two genuinely distinct phases of active matter.

The transition between these two dynamical phases is captured by the global polarization $\mathcal{P} \equiv \mathcal{P}(\ell = 2R)$, where R is the chamber radius. We can see in Fig. 2*B* that $\mathcal{P}$ decays weakly and linearly with Φ_o for small disorder but drops sharply to 0 at the critical value Φ_c defined from the proliferation of quenched topological defects in Fig 1*F*. The bifurcation of $\mathcal{P}$ in Fig. 2*B* suggests a critical scenario. This hypothesis is further supported by Fig. 2*C*, which reveals a divergence, or at the very least a drastic increase of the correlation length $\xi_{\mathcal{P}}$ at the onset of meandering motion. The polarization $\mathcal{P}$ alone, however, does not distinguish the meander from the gas phase. We thus introduce the Edwards–Anderson parameter $\mathcal{Q}_{EA} = \langle \hat{\mathbf{v}}(\mathbf{r}, t) \cdot \hat{\mathbf{v}}(\mathbf{r}, t + T)\rangle_{\mathbf{r},t,T\to\infty}$ that quantifies the temporal persistence of the emergent flows (41) (see also *SI Appendix*, section 2). The finite

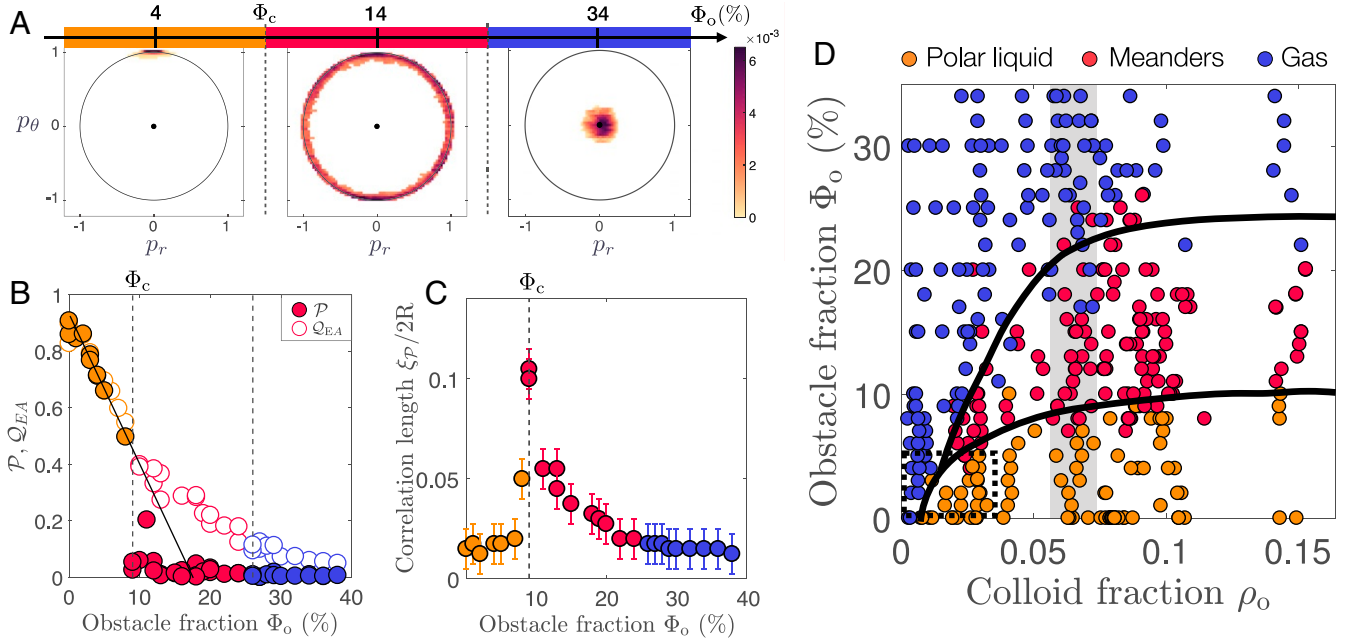

Fig. 2. Suppression of long-range orientational order. (*A*) Probability Distribution Function (PDF) of the polarization fields $P(p_r, p_\theta)$ in the three dynamical phases. Note that the distribution is isotropic but peaked along the unit circle in the meander phase: spontaneous flows are locally preserved but global polar order is suppressed by disorder. (*B*) Variation of the global polarization $\mathcal{P}$ and Edwards–Anderson $\mathcal{Q}_{EA}$ order parameters. In polar liquids $\mathcal{P} > 0$, in meanders $\mathcal{P} = 0$ but $\mathcal{Q}_{EA} > 0$, and in a gas both $\mathcal{P}$ and $\mathcal{Q}_{EA}$ vanish. The solid line corresponds to our theoretical prediction using β_o as a fitting parameter (Eq. **4**). The Toner–Tu hydrodynamic coefficients are estimated from ref. 37. We find $\beta_o \sim 1.6\beta$, which confirms the predictive power of our theory. The obstacles indeed have a dielectric constant comparable to the rollers' and a 1.5 larger volume, leading to comparable electrostatic repulsions (see ref. 6). (*C*) Correlation length of the polarization field defined from the exponential decay of $\mathcal{P}(\ell)$ plotted in *SI Appendix*, Fig. S1. The cusp of the $\xi_{\mathcal{P}}(\Phi_o)$ curve at Φ_c hints toward a critical dynamical transition. The accuracy in the measurement of $\xi/2R$ is of the order of 10^{-2}. (*D*) Phase diagram of polar active matter in isotropic disorder. The phase boundaries are equivalently determined from the number of topological defects (Fig. 1*F*), or from the variations of $\mathcal{P}$ and $\mathcal{Q}_{EA}$. In practice, we define the boundary separating the polar-liquid from the meander phase as $\mathcal{P} > 0.45$ and the boundary between the meander and gas phases as $\mathcal{P} < 0.45$ and $Q_{EA} > 0.2$. The geometry of the phase boundaries does not crucially depend on these criteria. The extent of the meander phase becomes vanishingly small only at the onset of the flocking transition. The dashed rectangle indicates the region of the phase diagram explored in ref. 22 where the meander phase was missed. Orientational order is generically lost due to the emergence of meander patterns. The gray rectangle corresponds to the series of experiments discussed in the main text.

nonzero value of $\mathcal{Q}_{\mathrm{EA}}$ for $\Phi_c < \Phi_o < 26\,\%$ (Fig. 2*B*) confirms the persistence of polar order along the meanders (42). We also find that the continuous transition, or cross-over, between the meander and the gas phase, where $\mathcal{Q}_{\mathrm{EA}} \sim 0$, coincides with that identified from the topological defect statistics in Fig. 1*F*.

Taking advantage of our high-content microfluidic experiments, we measure $\mathcal{P}$ and $\mathcal{Q}_{\mathrm{EA}}$ in more than 450 experiments performed varying the roller fraction from 10^{-3} to 1.5×10^{-1} and Φ_o from 0 to 38 % for multiple disorder realizations initial conditions, and obstacle size (*SI Appendix*). The resulting phase diagram shown in Fig. 2*D* firmly establishes that disorder and topological defects do not merely offset the flocking transition as reported in ref. 22 but conspire to bend the dynamics of polar liquids into amorphous and singular flows while preserving local flocking motion.

Meander Flows Are Dynamical Vortex Glasses

We now establish that the meanders realize a dynamical vortex glass. To do so, we compare the flow orientations of 50 replicas of the very same experiment ($\Phi_o = 15\,\%$). We solely vary the initial conditions, keeping the colloid fraction and disorder realization identical. We then quantify the resemblance between the flow patterns by introducing a measure of the local overlap $q_{\alpha\beta}(\mathbf{r}) = \boldsymbol{p}_\alpha(\mathbf{r}) \cdot \boldsymbol{p}_\beta(\mathbf{r})$ between replicas α and β. Examples of overlap maps are shown in Fig. 3*A* for four different pairs of experiments (see also *SI Appendix*, Fig. S7).

The replicated flows are identical when $q_{\alpha\beta}(\mathbf{r}) = +1$, opposite when $q_{\alpha\beta}(\mathbf{r}) = -1$, and orthogonal when $q_{\alpha\beta}(\mathbf{r}) = 0$. A simple inspection of the maps readily indicates that, although all experiments correspond to overall different patterns, a few macroscopic regions are virtually identical from one replica to another. More quantitatively, we plot in Fig. 3*C* the distribution of the global overlap $\mathcal{Q}_{\alpha\beta} = \langle q_{\alpha\beta}(\mathbf{r}) \rangle_{\mathbf{r}}$ and compare it to that of the macroscopic vortex obtained in the flocking state. The two distributions are markedly different. In the flocking state, $\mathrm{P}(\mathcal{Q}_{\alpha\beta})$ is composed of two symmetric peaks at $\mathcal{Q}_{\alpha\beta} = \pm 1$, as global circulations of either handedness are equally probable. Conversely, in the meander phase, $\mathrm{P}(\mathcal{Q}_{\alpha\beta})$ is not symmetric. It is a broad Gaussian distribution centered around a positive mean value. In other words, even though disorder is isotropic and homogeneous, we find that the local heterogeneities in the obstacle distribution bias the orientation of the flow field over macroscopic regions of space. As a result, reversing the orientation of the flow does not yield an equally probable pattern. The bias in the flow structure is clearly visible in the velocity field, which does not average to zero when averaged over all replicas (Fig 3*B*).

Crucially, the large width of the overlap distribution demonstrates a broad range of meandering patterns that do not merely differ from each other by continuous distortions. The replicas are actually topologically inequivalent, as demonstrated by the distribution of the difference in the number of topological defects between each pair of replicas ($\mathcal{N}_\alpha - \mathcal{N}_\beta$). The regions of the flow patterns that are robust to variations in the initial conditions are therefore shaped by pinned defects of identical charge and orientation which persist in all replicas. In other words, defects are strongly correlated not only in their spatial location but also in their flow direction. This becomes evident upon inspecting the statistics of local overlap.

Unlike the global overlap distribution, $\mathrm{P}(q_{\alpha\beta}(\mathbf{r}))$ is bimodal and sharply peaks at $q_{\alpha\beta}(\mathbf{r}) = \pm 1$ (Fig. 3*E*). Simply put, the meanders in each pair of replicas differ by the reversal of the flow orientation over a finite fraction of space. This area fraction is given by $1 - [\mathrm{P}(q_{\alpha\beta} = +1) - \mathrm{P}(q_{\alpha\beta} = -1)] \sim 0.5$ (see also *SI Appendix*, section 5). We can then estimate the typical extent

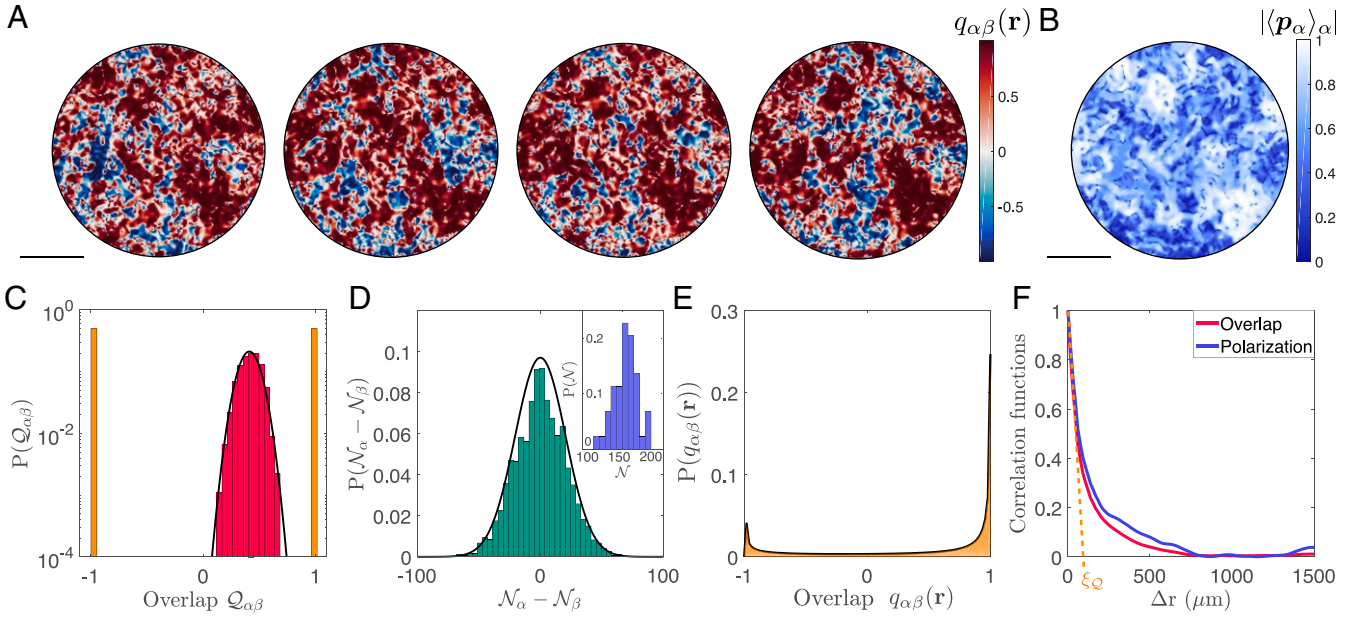

Fig. 3. Meanders as dynamical vortex glasses. (*A*) Maps of the overlap field $q_{\alpha\beta}(\mathbf{r})$ for 4 out of 1,225 different pairs of replicas (α, β). (Scale bar: 1 mm.) (*B*) Magnitude of the replica-averaged polarization field. Disorder robustly sets the flow orientation in macroscopic regions (light colors). (Scale bar: 1 mm.) (*C*) Overlap distributions in the polar liquid and meander phases. In the polar liquid phase (light orange) the distribution is symmetric and bimodal. Clockwise and counterclockwise vortices are equiprobable. In the meander phase, the distribution is a wide Gaussian centered on 0.46. (*D*) Distribution of the difference between the number of topological defects in each pair of replicas. The distribution is a Gaussian with a standard deviation $\sigma = 18 \pm 3$, much larger than the uncertainty defined by the standard deviation of the topological charge (which should be constrained to equal 1 in a circular geometry). (*Inset*) Distribution of the number of defects in each replica. The replicated flows are topologically distinct. (*E*) Probability density of the local overlap $q_{\alpha\beta}(\mathbf{r})$. The distribution is asymmetric but sharply peaked at ± 1. Locally the active fluid either flows along identical or opposite directions in each replica of the same experiment. (*F*) Decay of the spatial correlation of $q_{\alpha\beta}(\mathbf{r})$ averaged over all replicas and of the replica-averaged polarization field plotted in *B*. Both decorrelations occur over the same finite distance $\xi_{\mathcal{Q}} = 100 \pm 10$ μm. All panels correspond to experiments performed deep in the meander phase $\Phi_o = 15\,\%$.

of the compact regions where the flow can flip sign from one replica to another by measuring the correlation length of the local overlap or of the replica-averaged flow shown in Fig. 3*F*. We find that the overlap decorrelates exponentially over a finite distance $\xi_{\mathcal{Q}} = 100 \pm 10\,\mu\text{m}$. This finite correlation length implies that the meanders explore a conformational landscape including a number of steady states that scales as $\sim 2^{(R/\xi_{\mathcal{Q}})^2}$. The exponential degeneracy of the flows demonstrates that the meander phase is the dynamical analogue of a topological defect glass. It is strongly reminiscent of the vortex glass phases found in disordered flux lines in superconductors and in random-gauge Heisenberg magnets (28, 29, 43).

Dynamical Vortex Glass as a Gauge Glass

We now make a precise connection between the dynamical vortex glass we observe here in active fluids and its static counterpart in superconductors.

To do so, we construct a hydrodynamic theory of disordered polar flows, building on a final set of experiments performed in periodic lattices of obstacles (see *SI Appendix*, Fig. S8 and Movie S7). A systematic investigation reveals that no meander forms in the absence of disorder (see *SI Appendix*, section 6). The spatial heterogeneities in the local obstacle fraction $\phi_o(\mathbf{r})$ are essential to generate the meandering flow patterns. At lowest order in gradients, disorder thus minimally alters Toner–Tu hydrodynamics for the conserved roller density ρ and the flow velocity $\mathbf{v}$ (1, 34):

$$\partial_t \rho = -\boldsymbol{\nabla}\cdot(\rho\mathbf{v}), \qquad [1]$$

$$\partial_t \mathbf{v} + \lambda\mathbf{v}\cdot\boldsymbol{\nabla}\mathbf{v} = (a_2 - a_4|\mathbf{v}|^2)\mathbf{v} + K\nabla^2\mathbf{v} - \beta\boldsymbol{\nabla}\rho - \beta_o\boldsymbol{\nabla}\phi_o\,, \qquad [2]$$

All of the transport coefficients are taken to be constant positive parameters. When $\boldsymbol{\nabla}\phi_o = \mathbf{0}$, Eq. **2** reduces to the standard Toner–Tu equations, which quantitatively predict the vortical flows of Fig. 1*A* (32). The terms a_2, a_4 set the mean value of the flow velocity ($v_0 = \sqrt{a_2/a_4}$) deep in the homogeneous ordered phase, while λ controls self-advection and the elastic constant K penalizes flow distortions.

The β and β_o terms originate from the repulsive interactions between the rollers and between the rollers and obstacles, respectively. The β term is akin to the pressure gradient in compressible fluid flows, while $-\beta_o\boldsymbol{\nabla}\phi_o$ acts as a quenched random pressure gradient repelling the fluid away from the regions of high obstacle density. This equation provides a direct qualitative explanation for the bias of the overlap distribution in Fig. 3*C*. Although the obstacles are isotropic and, on average, homogeneously distributed, the repulsive interactions with the obstacles locally drives flows in the direction opposite to $\boldsymbol{\nabla}\phi_o$ in all replicas.

For weak disorder ($\Phi_o < \Phi_c$), the ordered flows are only marginally perturbed by the obstacles. As detailed in *SI Appendix*, section 7, we can then perform a simple linearized analysis about the polarized state, deep in the order phase where $\mathbf{v} = v_0(\cos\theta, \sin\theta)$. We readily obtain the steady state orientational correlator in Fourier space:

$$\overline{\theta_{\mathbf{q}}^2} = \frac{\beta_o^2 q_x^2 q_y^2}{[(c_\parallel v_0 q_x^2 - c_\perp^2 q_y^2)^2 + v_0^2 K^2 q_x^2 q^4]}\Phi_o\,, \qquad [3]$$

where the overbar denotes a disorder average. $c_\parallel = \lambda v_0$ and $c_\perp = \sqrt{\beta\rho_0}$ are the longitudinal and transverse sound speeds, respectively, and ρ_0 is the mean colloidal roller density. Velocity fluctuations hence remain finite on large scales signaling true long-range order. Eq. **3** quantitatively accounts for the linear decay of the polarization $\mathcal{P}(\Phi_o)$ below Φ_c, and the slope provides a measurement of the disorder strength: $\beta_o = 12.6 \pm 1.1\,\text{mm}^2.s^{-2}$ (see Fig. 2*B* and legend and *SI Appendix*, section 7.A.2).

For strong disorder we have to go beyond this spin-wave theory and account for both nonlinearities and the presence of topological defects. Unlike in equilibrium ferromagnets and active-nematic films, two-dimensional colloidal flocks support genuine long-range order, thereby ruling out the classical Kosterlitz–Thouless picture of defect unbinding. Topological defects in clean polar flocks only participate in a rapid coarsening process by annihilating quickly to yield pristine ordered flow, as evidenced in Fig. 1*A*. Disorder changes this picture in important ways. Quenched fluctuations due to the random obstacles provides an additional contribution that competes with orientational elasticity to uncover a new active defect-unbinding scenario. For simplicity, we fix the colloidal roller density to be a constant ($\rho = \rho_0$); the sole hydrodynamic mode is therefore the orientation θ. As detailed in *SI Appendix*, sections 8 and 9, retaining the full nonlinear dependence on θ in Toner–Tu equations we find that at long-wavelengths the convective nonlinearities solely compete with the random pressure term in Eq. **2**. To gain some insight into this competition, let us first consider a local minimum of $\phi_o(\mathbf{r})$ at the origin; the inward disorder pressure must be balanced by a centrifugal kinematic pressure $\sim \lambda v^2/r$ associated with an azimuthal flow. In a more general setting, the competition between convection and random pressure constrains the angular fluctuations to obey

$$\boldsymbol{\nabla}\theta = -\frac{\beta_o}{\lambda v_0^2}\hat{\mathbf{z}}\times\mathbb{P}\cdot\boldsymbol{\nabla}\phi_o \equiv \mathcal{A}(\mathbf{r})\,, \qquad [4]$$

where $\mathbb{P} = \mathbf{1} - \hat{\mathbf{v}}\hat{\mathbf{v}}$. Remarkably, this quenched distribution of phase distortions is reminiscent of random-gauge XY models, and flux-line glasses in type II superconductors (see, e.g., refs. 27–29). Eq. **4** reveals that active self-advection nonlinearly transforms the quenched disorder potential ϕ_o into an effective random gauge vector field $\mathcal{A}$. The local circulation of $\mathcal{A}$ then defines a quenched topological charge in the background $Q(\mathbf{r}) = \hat{\mathbf{z}}\cdot[\boldsymbol{\nabla}\times\mathcal{A}(\mathbf{r})]$.

For a given disorder configuration the flow streamlines on large scales must satisfy the nonlinear constraint in Eq. **4**, which can be used to obtain the steady-state distribution of θ to be $\mathrm{P}[\theta(\mathbf{r})] \propto \lim_{T\to 0}\exp(-E/T)$ with an auxiliary temperature T and an effective energy (see *SI Appendix*, section 8 for details):

$$E[\theta(\mathbf{r})] = \frac{K}{2}\int \mathrm{d}^2 r\,|\boldsymbol{\nabla}\theta - \mathcal{A}(\mathbf{r})|^2. \qquad [5]$$

The zero-temperature ground state controls the flow configurations of the disordered flock ($T \to 0$). This completes our mapping of the nonlinear meandering flows in a polar fluid on a disordered substrate to the well-known problem of finding the ground states of a random-gauge XY model (27, 29, 44).

The effective energy in Eq. **5** captures the competition between disorder generating meanders dictated by $\mathcal{A}$ and elastic restoring forces penalizing these distortions. This allows a Kosterlitz–Thouless-style argument for proliferating free vortices detailed in *SI Appendix*, section 9. We stress, however, the essential role of activity in our analysis. Although we obtain an equilibrium-like mapping in Eq. **5**, activity is crucial in generating the gauge field $\mathcal{A}$ via self-advection. Noting a the vortex-core size, the elastic penalty of an isolated defect $\sim K\ln(R/a)$ can be offset by the energy gain $\sim K\Phi_o(\beta_o/\lambda v_0^2)\ln(R/a)$ from optimally screening out the background charge. Their balance hence explains the central observation reported in Fig. 1*F*: There exists a finite threshold $\Phi_c \propto \lambda v_0^2/\beta_o$ beyond which pinned vortices can proliferate. Taking into account all numerical prefactors, and estimating the hydrodynamic parameters of Eq. **2** using active-sound spectroscopy (37), our minimal theory does not

include any free fitting parameter and predicts a critical fraction $\Phi_c \sim 3\%$, which is in reasonable agreement with the measured value ($\Phi_c = 9 \pm 1\%$) given the simplicity of our model (see *SI Appendix*, section 9). This prediction rationalizes the existence of the dynamical vortex glass phase along with its phase transition as being driven by disorder-induced unbinding of ± 1 vortices.

Concluding Remarks

In conclusion, combining high-content experiments and theory we have shown how dynamical vortex glasses generically emerge when the polar order of flocking matter competes with isotropic disorder. We emphasize the generality of our predictions. Both the topological-defect stabilization scenario and the extensive complexity of the flow patterns solely rely on stable uniaxial order in a fluid assembled from motile units. Beyond the specifics of colloidal active matter we therefore expect dynamical vortex glasses to emerge in a host of active materials ranging from confined microtubule nematics (11) to concentrated bacteria suspensions (38) and cell tissues (45) cruising through disorder. Establishing a quantitative theory of their amorphous patterns remains a formidable challenge.

Materials and Methods

Quincke Rollers Experiments. The experimental setup is similar to that described in ref. 37. We disperse polystyrene colloids of radius $a = 2.4\ \mu$m (G0500; Thermo Scientific) in a solution of hexadecane including 5.5×10^{-2} wt % of dioctyl sulfosuccinate sodium salt. We then inject the solution in microfluidic chambers made of two electrodes spaced by a 25-μm-thick Scotch tape. The electrodes are glass slides, coated with indium tin oxide (thickness 80 nm, ITOSOL30; Solems). We let the colloids sediment on the bottom electrode and apply a direct current (DC) voltage of 120 V. The resulting electric field triggers the so-called Quincke electrorotation and causes the colloids to roll at a constant speed $v_0 = 0.8$ mm/s (6, 46). The microfluidic device is sketched in Fig. 1*B*. We confine the colloidal rollers inside circular chambers of radius $R = 1.5$ mm including random lattices of circular posts of radius 5 μm. Both the obstacles and the confining disks are made of a 2-μm-thick layer of insulating photoresist resin (MICROPOSIT S1818) patterned by conventional UV lithography as explained in ref. 22. The patterns are lithographed on the bottom electrode. The distribution of the obstacle centers corresponds to a planar Poisson process and is therefore devoid of any spatial correlation. The circular posts can overlap as seen in Fig. 1*C* and Movie S3. The experiments reported in the main text correspond to 30 different microfluidic chambers including obstacle fractions ranging from 0 % to 38 %. We fine-tune the mean roller fraction ρ_0 using a T-junction to inject sequentially a colloidal suspension or a colloid-free solvent.

If not specified otherwise, the stationary flows are measured in the first chamber 120 s after the application of the DC field. This waiting time is more than one order of magnitude larger that the flows' relaxation time (see *SI Appendix*, section 2). For the replica experiments we proceed as follows. The chambers are filled with the colloids at the desired area fraction. We motorize the colloids, wait for 120 s, and film their motion for 5 s. We then switch the voltage off and switch it on again, repeating the same procedure 50 times in a row.

From Lagrangian Trajectories to Eulerian Flow Fields. In order to track the trajectories of the rollers, we image them with a Nikon AZ100 microscope with a 4.8× magnification and record videos with a Basler Ace camera at 190 frames per second. All measurements are systematically repeated three times for different initial conditions and the same disorder configuration. If not specified otherwise, we measure all quantities reported in the main text after the ensemble of rollers has reached its stationary state.

Lagrangian Trajectories. We detect the position of all of the rollers with a subpixel accuracy using the algorithm introduced by Lu et al. (47). We then reconstruct their trajectories over the whole 3-mm-wide circular chambers using the Crocker and Grier algorithm (48) with the MATLAB routine available in ref. 49. We define the individual roller velocities from their displacements over two subsequent frames (time interval: $\delta t = 5.3$ ms): $\mathbf{v}_i(t) = \mathbf{r}_i(t + \delta t) - \mathbf{r}_i(t)$, where $\mathbf{r}_i(t)$ and $\mathbf{v}_i(t)$ are, respectively, the position and velocity of particule i at time t. The accuracy of the position measurements is of the order of 0.1 μm, inducing an accuracy of the order of 40 μm/s for individual speed measurements. When powered with an electric field $\mathbf{E}$ of magnitude 120 V, all colloids roll at a constant speed:

$$v_0 = 0.80 \pm 0.04\ \text{mm/s}. \qquad [6]$$

In addition, when isolated, their direction of motion freely diffuses on the unit circle with a rotational diffusivity D_R defined as the exponential decorrelation rate of the velocity orientation in an isotropic phase:

$$D_R = 2.2 \pm 0.1\ \text{s}^{-1}. \qquad [7]$$

Eulerian Fields. Building on these Lagrangian measurements, we reconstruct the instantaneous Eulerian velocity fields $\mathbf{v}(\mathbf{r}, t)$ as follows. We average the instantaneous roller velocities in 76.4-μm × 76.4-μm binning windows arranged on a square lattice with a lattice spacing of 15.3 μm. Given the roller density, each particle image velocimetry window typically averages the velocity of 25 rollers. We systematically checked that none of our results qualitatively depends on the specific choice of the size of the binning windows. The polarization and overlap fields are computed with the same spatial resolution from $\mathbf{v}(\mathbf{r}, t)$.

To compute the polarization order parameter from the instantaneous velocity field, we first average the radial and azimuthal components of the polarization field $\boldsymbol{p}(\mathbf{r}) \equiv \langle \hat{\mathbf{v}}(\mathbf{r}, t) \rangle_t$ over square boxes of size ℓ. We then compute the spatial average: $\boldsymbol{p}_B \equiv (\langle p_r(\mathbf{r}) \rangle_\mathbf{r}, \langle p_\theta(\mathbf{r}) \rangle_\mathbf{r})$, in each box B. Finally, $\mathcal{P}(\ell)$ corresponds to the norm of $\boldsymbol{p}_B$ averaged over all boxes B.

Data Availability. Fig. 1 data have been deposited in FigShare (https:/doi.org/10.6084/m9.figshare.12887180.v1).

ACKNOWLEDGMENTS. We acknowledge support from the Agence Nationale de la Recherche program Wave Topology in Fluids and the Initiative of Excellence program ToRe. M.C.M. was supported by NSF award DMR-1938187. S.S. is supported by the Harvard Society of Fellows. We thank L. Berthier, D. Carpentier, H. Chaté, O. Dauchot, B. Mahault, A. Morin, and T. M. Irvine for insightful comments and suggestions.

1. J. Toner, Y. Tu, S. Ramaswamy, Hydrodynamics and phases of flocks. *Ann. Phys.* **318** (1), 170–244 (2005).
2. M. C. Marchetti *et al.*, Hydrodynamics of soft active matter. *Rev. Mod. Phys.* **85**, 1143–1189 (2013).
3. A. Cavagna, I. Giardina, Bird flocks as condensed matter. *Annu. Rev. Condens. Matter Phys.* **5**, 183–207 (2014).
4. H. Chaté, Dry aligning dilute active matter. *Annu. Rev. Condensed Matter Phys.* **11**, 189–212 (2020).
5. V. Schaller, C. Weber, C. Semmrich, E. Frey, A. R. Bausch, Polar patterns of driven filaments. *Nature* **467**, 73–77 (2010).
6. A. Bricard, J. B. Caussin, N. Desreumaux, O. Dauchot, D. Bartolo, Emergence of macroscopic directed motion in populations of motile colloids. *Nature* **503**, 95–98 (2013).
7. J. Yan *et al.*, Reconfiguring active particles by electrostatic imbalance. *Nat. Mater.* **15**, 1095–1099 (2016).
8. J. Zhang, E. Luijten, B. A. Grzybowski, S. Granick, Active colloids with collective mobility status and research opportunities. *Chem. Soc. Rev.* **46**, 5551–5569 (2017).
9. J. Deseigne, S. Léonard, O. Dauchot, H. Chaté, Vibrated polar disks: Spontaneous motion, binary collisions, and collective dynamics. *Soft Matter* **8**, 5629–5639 (2012).
10. N. Kumar, H. Soni, S. Ramaswamy, A. Sood, Flocking at a distance in active granular matter. *Nat. Commun.* **5**, 4688 (2014).
11. A. Doostmohammadi, J. Ignés-Mullol, J. M. Yeomans, F. Sagués, Active nematics. *Nat. Commun.* **9**, 3246 (2018).
12. S. Shankar, S. Ramaswamy, M. C. Marchetti, Low-noise phase of a two-dimensional active nematic system. *Phys. Rev.* **97**, 012707 (2018).
13. T. Sanchez, D. T. N. Chen, S. J. DeCamp, M. Heymann, Z. Dogic, Spontaneous motion in hierarchically assembled active matter. *Nature* **491**, 431–434 (2012).
14. L. Giomi, M. J. Bowick, X. Ma, M. C. Marchetti, Defect annihilation and proliferation in active nematics. *Phys. Rev. Lett.* **110**, 228101 (2013).
15. S. Shankar, S. Ramaswamy, M. C. Marchetti, M. J. Bowick, Defect unbinding in active nematics. *Phys. Rev. Lett.* **121**, 108002 (2018).
16. J. A. Blackman, J. Tagüeña, *Disorder in Condensed Matter Physics: A Volume in Honour of Roger Elliott* (Oxford University Press, 1991).
17. P. G. De Gennes, *Superconductivity of Metals and Alloys* (CRC Press, 2018).
18. G. W. Crabtree, D. R. Nelson, Vortex physics in high-temperature superconductors. *Phys. Today* **50**, 38–45 (1997).
19. O. Chepizhko, E. G. Altmann, F. Peruani, Optimal noise maximizes collective motion in heterogeneous media. *Phys. Rev. Lett.* **110**, 238101 (2013).
20. D. A. Quint, A. Gopinathan, Topologically induced swarming phase transition on a 2d percolated lattice. *Phys. Biol.* **12**, 046008 (2015).
21. C. Bechinger *et al.*, Active particles in complex and crowded environments. *Rev. Mod. Phys.* **88**, 045006 (2016).

22. A. Morin, N. Desreumaux, J. B. Caussin, D. Bartolo, Distortion and destruction of colloidal flocks in disordered environments. *Nat. Phys.* **13**, 63–67 (2017).
23. R. Das, M. Kumar, S. Mishra, Polar flock in the presence of random quenched rotators. *Phys. Rev. E* **98**, 060602 (2018).
24. C. O. Reichhardt, C. Reichhardt, Avalanche dynamics for active matter in heterogeneous media. *New J. Phys.* **20**, 025002 (2018).
25. J. Toner, N. Guttenberg, Y. Tu, Swarming in the dirt: Ordered flocks with quenched disorder. *Phys. Rev. Lett.* **121**, 248002 (2018).
26. J. Toner, N. Guttenberg, Y. Tu, Hydrodynamic theory of flocking in the presence of quenched disorder. *Phys. Rev. E* **98**, 062604 (2018).
27. M. Rubinstein, B. Shraiman, D. R. Nelson, Two-dimensional XY magnets with random Dzyaloshinskii-Moriya interactions. *Phys. Rev. B* **27**, 1800 (1983).
28. T. Nattermann, S. Scheidl, Vortex-glass phases in type-ii superconductors. *Adv. Phys.* **49**, 607–704 (2000).
29. D. Carpentier, P. Le Doussal, Topological transitions and freezing in XY models and Coulomb gases with quenched disorder: Renormalization via traveling waves. *Nucl. Phys. B* **588**, 565–629 (2000).
30. G. Quincke, Ueber Rotationen im Constanten Electrischen Felde. *Ann. Phys.* **295**, 417–486 (1896).
31. O. D. Lavrentovich, Active colloids in liquid crystals. *Curr. Opin. Colloid Interface Sci.* **21**, 97–109 (2016).
32. A. Bricard *et al.*, Emergent vortices in populations of colloidal rollers. *Nat. Commun.* **6**, 7470 (2015).
33. D. Geyer, D. Martin, J. Tailleur, D. Bartolo, Freezing a flock: Motility-induced phase separation in polar active liquids. *Phys. Rev. X* **9**, 031043 (2019).
34. J. Toner, Y. Tu, Long-range order in a two-dimensional dynamical XY model: How birds fly together. *Phys. Rev. Lett.* **75**, 4326–4329 (1995).
35. M. Zeitz, K. Wolff, H. Stark, Active Brownian particles moving in a random Lorentz gas. *Euro. Phys. J. E* **40**, 23 (2017).
36. A. Morin, D. Lopes Cardozo, V. Chikkadi, D. Bartolo, Diffusion, subdiffusion, and localization of active colloids in random post lattices. *Phys. Rev. E* **96**, 042611 (2017).
37. D. Geyer, A. Morin, D. Bartolo, Sounds and hydrodynamics of polar active fluids. *Nat. Mater.* **17**, 789–793 (2018).
38. H. Wioland, E. Lushi, R. E. Goldstein, Directed collective motion of bacteria under channel confinement. *New J. Phys.* **18**, 075002 (2016).
39. K. T. Wu *et al.*, Transition from turbulent to coherent flows in confined three-dimensional active fluids. *Science* **355**, eaal1979 (2017).
40. A. Opathalage *et al.*, Self-organized dynamics and the transition to turbulence of confined active nematics. *Proc. Natl. Acad. Sci. U.S.A.* **116**, 4788–4797 (2019).
41. A. Cavagna, Supercooled liquids for pedestrians. *Phys. Rep.* **476**, 51–124 (2009).
42. Y. Duan, B. Mahault, Yq. Ma, Xq. Shi, H. Chaté, Breakdown of ergodicity and self-averaging in polar flocks with quenched disorder. arXiv [Preprint] (2020). https://arxiv.org/abs/2010.02356 (Accessed 5 October 2020).
43. M. P. A. Fisher, Vortex-glass superconductivity: A possible new phase in bulk high-t_c oxides. *Phys. Rev. Lett.* **62**, 1415–1418 (1989).
44. D. Carpentier, P. Le Doussal, Disordered XY models and Coulomb gases: Renormalization via traveling waves. *Phys. Rev. Lett.* **81**, 2558 (1998).
45. G. Duclos *et al.*, Spontaneous shear flow in confined cellular nematics. *Nat. Phys.* **14**, 728–732 (2018).
46. J. R. Melcher, G. I. Taylor, Electrohydrodynamics: A review of the role of interfacial shear stresses. *Annu. Rev. Fluid Mech.* **1**, 111–146 (1969).
47. P. J. Lu, P. A. Sims, H. Oki, J. B. Macarthur, D. A. Weitz, Target-locking acquisition with real-time confocal (TARC) microscopy. *Optic Express* **15**, 8702–8712 (2007).
48. J. C. Crocker, D. G. Grier, Methods of digital video microscopy for colloidal studies. *J. Colloid Interface Sci.* **179**, 298–310 (1996).
49. D. Blair, E. Dufresne, The Matlab particle tracking code repository. physics.georgetown.edu/matlab/. Accessed 1 September 2018.